Received: 13 December 2018 | Revised: 4 March 2019 | Accepted: 8 April 2019

DOI: 10.1002/mrm.27789

FULL PAPER

Magnetic Resonance in Medicine

Compressed Sensing 3D-GRASE for faster High-Resolution MRI

A. Cristobal-Huerta[1] | D.H.J. Poot[1,2] | M.W. Vogel[3] | G.P. Krestin[1] | J.A. Hernandez-Tamames[1]

[1]Department of Radiology and Nuclear Medicine, Erasmus MC, Rotterdam, The Netherlands

[2]Department of Medical Informatics, Erasmus MC, Rotterdam, The Netherlands

[3]GE Healthcare, Hoevelaken, The Netherlands

Correspondence
A. Cristobal-Huerta, Department of Radiology and Nuclear Medicine, Erasmus MC, Rotterdam, The Netherlands.
Email: a.cristobalhuerta@erasmusmc.nl

Purpose: High-resolution three-dimensional (3D) structural MRI is useful for delineating complex or small structures of the body. However, it requires long acquisition times and high SAR, limiting its clinical use. The purpose of this work is to accelerate the acquisition of high-resolution images by combining compressed sensing and parallel imaging (CSPI) on a 3D-GRASE sequence and to compare it with a (CS)PI 3D-FSE sequence. Several sampling patterns were investigated to assess their influence on image quality.

Methods: The proposed k-space sampling patterns are based on two undersampled k-space grids, variable density (VD) Poisson-disc, and VD pseudo-random Gaussian, and five different trajectories described in the literature. Bloch simulations are performed to obtain the transform point spread function and evaluate the coherence of each sampling pattern. Image resolution was assessed by the full-width at half-maximum (FWHM). Prospective CSPI 3D-GRASE phantom and in vivo experiments in knee and brain are carried out to assess image quality, SNR, SAR, and acquisition time compared to PI 3D-GRASE, PI 3D-FSE, and CSPI 3D-FSE acquisitions.

Results: Sampling patterns with VD Poisson-disc obtain the lowest coherence for both PD-weighted and T_2-weighted acquisitions. VD pseudo-random Gaussian obtains lower FWHM, but higher sidelobes than VD Poisson-disc. CSPI 3D-GRASE reduces acquisition time (43% for PD-weighted and 40% for T_2-weighted) and SAR (∼45% for PD-weighted and T_2-weighted) compared to CSPI 3D-FSE.

Conclusions: CSPI 3D-GRASE reduces acquisition time compared to a CSPI 3DFSE acquisition, preserving image quality. The design of the sampling pattern is crucial for image quality in CSPI 3D-GRASE image acquisitions.

KEYWORDS
compressed sensing and parallel imaging, CS, Echo planar imaging, Fast spin echo, GRASE, SAR

1 | INTRODUCTION

High-resolution three-dimensional (3D) structural MR imaging can accurately delineate complex or small structures of the body.[1] However, it requires long acquisition times, thereby limiting its clinical use.[2] To mitigate this drawback, a Fast Spin Echo (FSE) sequence is often used to acquire 3D high-resolution images.[2] Nevertheless, in FSE the speed and spatial coverage at high magnetic field strengths ($\geq$ 3T) is limited by the specific absorption rate (SAR).[3] This limitation is overcome by the Gradient and Spin Echo (GRASE) sequence,[4] since it combines a train of radiofrequency (RF) refocusing pulses, also called echo train (ET), with a train of bipolar readout gradients in between refocusing pulses. To accommodate the readout gradient, the spacing between RF refocusing pulses, or RF-spacing, is elongated for GRASE acquisitions compared with FSE acquisitions. Therefore, GRASE reduces SAR and may shorten image acquisition time compared to FSE. However, GRASE is prone to image artifacts due to phase and amplitude differences between spin-echo (SE) and gradient-recalled-echo (GRE),[5] and to the signal decay along the ET. To minimize these artifacts, several k-space trajectories for a variable flip angle algorithm (VFA) 3D-GRASE sequence have been proposed and evaluated.[6]

Imaging acquisition techniques can be combined with imaging reconstruction methods to achieve shorter scan times. Reconstruction methods rely on specific *a priori* information to obtain images from a reduced amount of measurements without degrading image quality. Parallel imaging (PI)[7] requires a regular undersampled k-space and a coil sensitivity map to obtain an artifact-free image. Image domain PI usually obtains the coil sensitivity map through an additional scan, while k-space PI requires a fully sampled k-space center, also called autocalibrated signal (ACS) region, to implicitly estimate the coil sensitivity map. Compressed sensing (CS)[8] allows reconstructing images from highly undersampled measurements, relying on the sparsity of the image in a transform domain, an incoherent sampling pattern, and a nonlinear reconstruction method.[8] CS has been combined with PI showing higher acceleration rates than each method by itself.[9,10] If CS and a k-space-based PI methods are combined (CSPI), the sampling pattern needs to acquire the ACS k-space region, required by PI, and also needs to lead to incoherent aliasing artifacts, as required by CS. Recently, CSPI has been successfully implemented in 3D-FSE for $T_{1_{rho}}$ imaging of the knee, obtaining comparable image quality in a shorter acquisition time.[11] For 3D-GRASE, we recently presented promising results on CSPI in knee[12] and brain imaging.[13]

The design of the sampling pattern is crucial for a successful CSPI reconstruction.[14] A CSPI sampling pattern comprises the design of the undersampled k-space grid and the trajectory, that is, specifying the k-space lines and the time order to be acquired. Several variable density (VD) undersampling k-space grids have been proposed to satisfy the incoherent sampling requirement of CSPI and to take also into account the energy distribution of the MR signal.[11,14,15] VD Poisson-disc or VD pseudo-random Gaussian k-space grids are among the most commonly and successfully used for this purpose. Theoretically, a VD Poisson-disc k-space grid is beneficial for both CS and PI reconstruction methods independently, as it avoids holes and clusters in the k-space grid.[16] However, a thoroughly study comparing both k-space grids has not been performed for brain and knee.

The effect of different sampling strategies for CSPI has mainly been assessed retrospectively by undersampling a fully sampled k-space to obtain the desired k-space grid.[17,18] These assessments usually do not take into account the trajectory, neglecting artifacts created by the difference in amplitude and phase of the k-space lines along the ET. Therefore, prospective assessments are essential in 3D-GRASE, where the trajectory plays an important role due to the differences in amplitude and phase between SE and GRE. For this reason, CSPI 3D-GRASE prospective studies investigating how different sampling patterns influence the image quality are required. Moreover, a CSPI 3D-GRASE acquisition strategy has not been introduced and explored until now.

The aim of this work is to propose and investigate an efficient CSPI acquisition strategy for the VFA 3D-GRASE sequence to reduce the acquisition time of high-resolution structural imaging compared to a CSPI 3D-FSE, maintaining image quality. Sampling patterns based on the VD Poisson-disc and VD pseudo-random Gaussian k-space grids and five different k-space trajectories described Cristobal-Huerta et al[6] are considered and evaluated. Bloch simulations are performed to obtain the transform point spread function (TPSF) and evaluate the degree of coherence of each sampling pattern. Finally, prospective CSPI 3D-GRASE phantom and prospective in vivo experiments in a knee and a brain were performed to assess the influence of each sampling pattern on the image quality and compared to PI 3D-GRASE, PI 3D-FSE, and CSPI 3D-FSE acquisitions.

2 | METHODS

2.1 | K-space sampling pattern design

The design of a k-space sampling pattern consists of two steps. First, the design must specify the k-space lines that should be acquired, here named as "k-space grid". Second, it must establish the time order on which each k-space line is acquired, here named as "trajectory".

In this section, the design of the k-space grid and the different trajectories to obtain PD-weighted and T_2-weighted images with 3D-GRASE is provided. Supporting Information Figures S1-S5 show examples of the different sampling patterns.

2.1.1 | K-space grid

Two VD cartesian undersampled k-space grids were investigated: VD pseudo-random Gaussian and VD Poisson-disc. The VD pseudo-random Gaussian k-space grid was generated according to the steps described in Pandit et al.[11] First, the k-space is regularly undersampled, as conventional for PI acquisitions. Afterward, the regular undersampled area is further undersampled in a random fashion, following a pseudo-random Gaussian distribution with standard deviation in each direction equal to the width of the acquisition matrix in that direction. In order to obtain a variable density distribution of k-space lines, the further undersampling was only performed outside an area slightly larger than the ACS region. Inside that region, the regular PI undersampling was preserved (see Figure 1A).

The VD Poisson-disc k-space grid was generated with the Berkeley Advanced Reconstruction Toolbox (BART).[19] An example of this k-space grid can be found in Figure 1B.

For the cases evaluated in this paper, the ACS region was set to approximately 2% of the total number of k-space lines in a full acquisition. Since more slices were acquired for T_2-weighted acquisitions, the ACS regions for this case was set to 27×27 ($k_y \times k_z$) k-space lines. For PD-weighted acquisitions, it was set to 21×21 ($k_y \times k_z$) k-space lines. The PI acceleration factor for both k-space grids was fixed to $k_y = 2$ and $k_z = 1$. For the pseudo-random Gaussian k-space grid, the area in which no further undersampling was performed was fixed empirically to 80×32 ($k_y \times k_z$). The overall acceleration factor, here named as CSPI acceleration factor, is the same for both k-space grids, thus, they acquire the same total number of k-space lines. To achieve this, the Poisson-disc k-space grid was first generated with the desired CSPI acceleration factor. Then, the pseudo-random Gaussian k-space grid was adjusted to the same CSPI acceleration factor by further undersampling the outer region of the k-space.

2.1.2 | Trajectories

The cartesian trajectories in Cristobal-Huerta et al[6] were used to establish the time order of each k-space line in the acquisition. These trajectories were designed to achieve the desired contrast while minimizing artifacts caused by small phase and amplitude differences between GRE and SE. Moreover, they do not require a fixed k-space grid, which allows using different CSPI k-space grids. Here, these trajectories are briefly explained. We refer the readers to Cristobal-Huerta et al[6] for a more detailed explanation of the implementation.

- *PD-weighted Trajectories* For PD-weighted images, it proposes the Segmented Radial Encoding (SRE) and the Segmented Linear Center-out Encoding (SLCE). The SRE trajectory combines the SORT phase-encoding[20] and the cartesian radial modulation[21] trajectories. The echoes from each GRE position are grouped concentrically, mixing T_2 relaxation and off-resonance effects along both k_y and k_z. The two modes, named as $M = 0$ and $M = 1$, modulate T_2 relaxation effects differently. The SLCE trajectory combines the SORT phase-encoding and the linear signal modulation.[21] It distributes off-resonance effects along k_z and

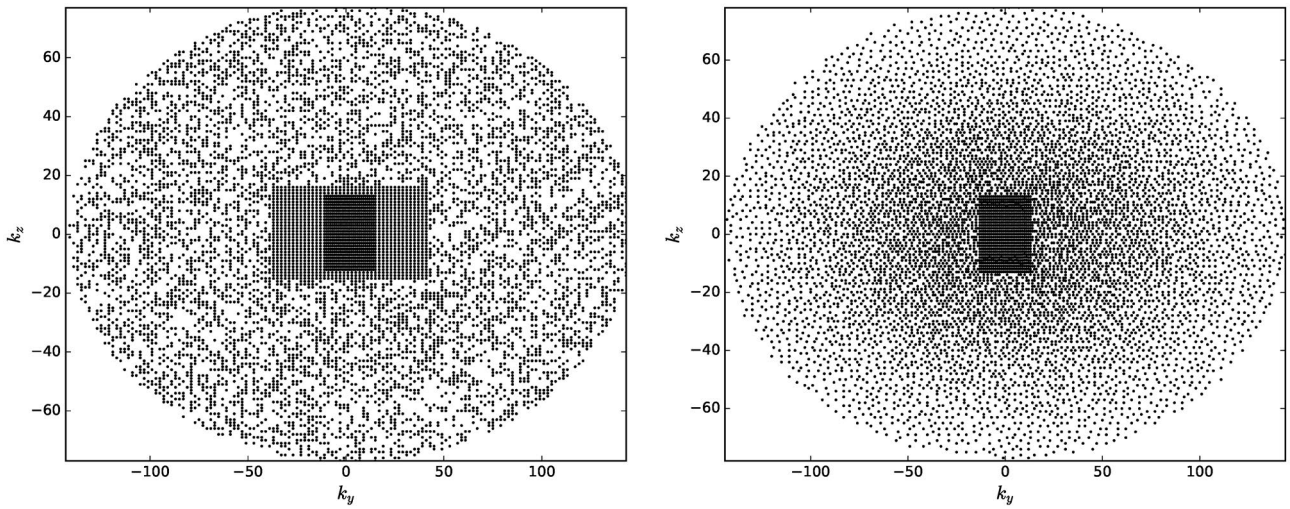

(A) Undersampled k-space grid using a VD pseudo-random Gaussian undersampling

(B) Undersampled k-space grid using a VD Poisson disk undersampling

FIGURE 1 Example of the proposed CSPI undersampled k-space grids. (A), Undersampled k-space grid using a variable density pseudo-random Gaussian undersampling and (B), Undersampled k-space grid using a variable density Poisson-disc undersampling. Both k-space grids have the same ACS region for PI

T_2 relaxation effects along k_y, filling the k-space outward along k_y. Two different alternatives were proposed, called SLCE 1 and SLCE 2. SLCE 1 alternates positive and negative k_y coordinates in each ET, while SLCE 2 alternates ET with only positive or only negative k_y coordinates.

- T_2-*weighted Trajectory* For T_2-weighted, the Segmented Linear Encoding (SLE) combines the SORT phase-encoding and the linear signal modulation[21] trajectories. This combination distributes off-resonance effects along k_z and T_2 relaxation effects along k_y to minimize artifacts.

2.2 | Reconstruction

In 3D-GRASE, phase correction is needed before the CSPI reconstruction to correct phase differences between SE and GRE. For this purpose, two reference ETs, one at the beginning and one at the end of the acquisition, were acquired without playing out slice and phase encoding gradients. GRE-SE phase differences in-between RF refocusing pulses were estimated for each position in the frequency encoding direction, for each coil individually, from the averaged reference scans. These phase differences were subsequently corrected in every ET of the acquisition.[5]

CSPI 3D-FSE and CSPI 3D-GRASE image reconstruction are performed by the l1-ESPIRiT reconstruction method implemented in the BART library.[22] First, coil sensitivity maps are computed by the ESPIRiT algorithm. Secondly, the images are reconstructed by the soft-SENSE algorithm with l1-wavelet regularization, with regularization parameter $\lambda = 0.01$. This λ was chosen heuristically to avoid either very smooth or noisy images.

For PI 3D-FSE and PI 3D-GRASE, image reconstruction is carried out by the Autocalibrating Reconstruction for Cartesian imaging (ARC) method.[23] A kernel of $7 \times 3 \times 3$ (x/y/z) was used to estimate missing k-space lines.

Afterward, magnitude images from each individual channel were combined by root sum of squares. Finally, vendor's provided correction for gradient nonlinearities was applied to each slice.

Both sequences followed the same image reconstruction process for all phantom and in vivo acquisitions, except for the phase correction, which was only applied to 3D-GRASE.

2.3 | Simulation experiments

Bloch simulations were carried out to study the degree of incoherence and the theoretical image resolution of each CSPI sampling pattern. The same Bloch simulations were also performed for each PI sampling pattern to evaluate the image resolution. The simulations were performed including T_2 decay, T_2^* decay and off-resonance effects (B0).

The transform point spread function (TPSF) was obtained for every sampling pattern following the procedure in Lustig et al[8] and Lustig et al[24]:

$$\mathrm{TPSF}(i,j) = \Sigma_{c,k} e_i^* \Psi C_c^* \mathcal{F}^* M_k^T s_k M_k \mathcal{F} C_c \Psi^* e_j, \qquad (1)$$

where Ψ is the wavelet transform, C_c is a diagonal matrix with the complex sensitivity of each coil c, $\mathcal{F}$ denotes the Fourier operator, M_k is a binary matrix selecting all k-space positions in echo k, s_k is the signal in echo k, and e_i and e_j are the i-th and j-th natural basis vectors. Due to computational constraints, for each sampling pattern the TPSF was evaluated for all j and 10 000 uniformly distributed pseudo-random i (wavelet coefficients). Since each wavelet level has different matrix sizes, the 10 000 coefficients were split in 375 wavelet coefficients for each of the sub-bands of the first level and 1000 wavelet coefficients for each of the sub-bands in the second level.

To measure the coherence on the TPSF, the mean side-lobe-to-peak ratio (SPR) of the TPSF was evaluated[8]:

$$\mathrm{SPR} = \frac{|\mathbf{d}^T \mathbf{n}|}{|\mathbf{d}^T \mathbf{d}|} \qquad (2)$$

$$\text{with } n_i = \max_{j \neq i} |\mathrm{TPSF}(i,j)| \text{ and } d_i = \mathrm{TPSF}(i,i).$$

To obtain s_k, the simulations used the in vivo acquisitions settings in Table 1 for PD-weighted sampling patterns, and Table 2 for T_2-weighted sampling patterns, except for the RF-spacing, for which the following values were used: for PD-weighted: 5.16 milliseconds (CSPI 3D-FSE) and 9.28 milliseconds (CSPI 3D-GRASE); for T_2-weighted: 4.56 milliseconds (CSPI 3D-FSE) and 8.07 milliseconds (CSPI 3D-GRASE). The properties of the simulated tissues were[25-27]: *White matter* (WM): $T_1 = 832$ milliseconds, $T_2 = 110$ milliseconds and $T_2^* = 45$ milliseconds B0 = 0 Hz; *White Matter B0* (WM B0): $T_1 = 832$ milliseconds, $T_2 = 110$ milliseconds and $T_2^* = 45$ milliseconds B0 = 50 Hz; *Grey matter* (GM): $T_1 = 1331$ milliseconds $T_2 = 79.6$ milliseconds and $T_2^* = 45$ milliseconds B0 = 0 Hz; *Grey matter B0*: $T_1 = 1331$ milliseconds, $T_2 = 79.6$ milliseconds and $T_2^* = 45$ milliseconds B0 = 50 Hz; *Cartilage* (CL): $T_1 = 1240$ milliseconds, $T_2 = 36.9$ milliseconds and $T_2^* = 22.6$ milliseconds B0 = 0 Hz; *Cartilage B0* (CL B0): $T_1 = 1240$ milliseconds, $T_2 = 36.9$ milliseconds and $T_2^* = 22.6$ milliseconds B0 = 50 Hz; *Bone Marrow* (BM): $T_1 = 371$ milliseconds, $T_2 = 133$ milliseconds and $T_2^* = 30$ milliseconds B0 = 0 Hz; *Bone Marrow B0* (BM B0): $T_1 = 371$ milliseconds, $T_2 = 133$ milliseconds and $T_2^* = 30$ milliseconds B0 = 50 Hz. The coil sensitivity maps, C_c, were obtained by the ESPIRiT algorithm from the ACR-Nema phantom[28] with an 8-channel head coil.

TABLE 1 Phantom and in vivo imaging acquisition parameters for PI 3D-FSE, CSPI 3D-FSE, PI 3D-GRASE, and CSPI 3D-GRASE PD-weighted knee images

	PDw knee									
	PI 3D-FSE	**CSPI 3D-FSE**	**PI 3D-GRASE**				**CSPI 3D-GRASE**			
					SRE				**SRE**	
	Radial modulation		**SLCE 1**	**SLCE 2**	$M = 0$	$M = 1$	**SLCE 1**	**SLCE 2**	$M = 0$	$M = 1$
TR (millisecond)	1200	1200	1200				1200			
TE (millisecond)	12.53	15.96	20.26	19.21	18.60	18.60	17.87	19.18/18.34	18.34/18.54	18.34/18.54
RF-spacing (millisecond)	4.98	5.17	9.98	9.47	9.17		8.80	9.46/9.04	9.04/9.14	9.04/9.14
ET length	27	27	16				16			
FOV (cm)	16	16	16				16			
EPI factor	1	1	3				3			
Receive bandwidth (kHz)	±100	±100	±100				±100			
Acquisition matrix	288 × 288 × 96	288 × 288 × 96	288 × 288 × 96				288 × 288 × 96			
Voxel size (mm)	0.55 × 0.55 × 1	0.55 × 0.55 × 1	0.55 × 0.55 × 1				0.55 × 0.55 × 1			
CSPI Acceleration factor	2.50	4.61	2.50				4.61			
Fat Saturation	Yes	Yes	Yes				Yes			
Time (min)	8:12	4:26	4:37	4:38	4:37	4:37	2:32	2:36	2:32	2:32
AveSAR ($\frac{W}{kg}$)	0.06	0.06	0.04				0.04			

Same parameters were used for PI and CSPI images acquisitions, except for TE, RF-spacing, and the acceleration factor. For CSPI, different TEs are obtained in the sampling patterns depending on the k-space grid (Variable Density Poisson-disc/Variable Density pseudo-random Gaussian). SAR values are shown for the first volunteer (weight = 70 Kg).

TABLE 2 Phantom and in vivo imaging acquisition parameters for PI 3D-FSE, CSPI 3D-FSE, PI 3D-GRASE, and CSPI 3D-GRASE T_2-weighted brain images

	T_2w brain			
	PI 3D-FSE	**CSPI 3D-FSE**	**PI 3D-GRASE**	**CSPI 3D-GRASE**
	Linear modulation		**SLE**	
TR (millisecond)	2800	2800	2800	2800
TE (millisecond)	73.42	74.75	77.07	78.78
ET length	94	94	53	53
RF-spacing (millisecond)	4.46	4.56	7.87	7.84/7.95
FOV (cm)	24	24	24	24
EPI factor	1	1	3	3
Receive bandwidth (kHz)	±62.5	±62.5	±100	±100
Acquisition matrix	288 × 288 × 156	288 × 288 × 156	288 × 288 × 156	288 × 288 × 156
Voxel size (mm)	0.83 × 0.83 × 1	0.83 × 0.83 × 1	0.83 × 0.83 × 1	0.83 × 0.83 × 1
CSPI Acceleration factor	2.5	5.65	2.5	5.65
Time (min)	8:58	3:52	5:19	2:20
AveSAR ($\frac{W}{kg}$)	0.71	0.71	0.41	0.41

Same parameters were used for PI and CSPI images acquisitions, except for TE, RF-spacing, and the acceleration factor. For CSPI, different TEs are obtained in the sampling patterns depending on the k-space grid (Variable Density Poisson-disc/Variable Density pseudo-random Gaussian). SAR values are shown for the first volunteer (weight = 70 Kg).

The position of the wavelet coefficients was different for PD-weighted simulations and T_2-weighted simulations, because of the different matrix sizes used in the protocols. However, the same coefficients were simulated for every sampling pattern within the PD-weighted sampling patterns and T_2-weighted sampling patterns.

Image resolution was assessed by the full width at half maximum (FHWM) of the point spread function (PSF) both in CSPI and PI sequences.

2.4 | Phantom experiment

Signal to noise ratio (SNR) and the no-reference perception-based image quality evaluator (PIQUE)[29] of every sampling pattern were assessed on the QA head SNR phantom (Model: 2321556, General Electric, GE, Milwaukee, WI). 3D-FSE and 3D-GRASE phantom images for each sampling pattern were acquired following the in vivo protocols showed in Tables 1 and 2 for PD-weighted and T_2-weighted images, respectively. Images were acquired in the sagittal plane, with frequency encoding direction S/I, on a 3T General Electric Discovery MR750 clinical scanner (General Electric Medical Systems, Waukesha, Wisconsin) with an eight-channel birdcage-like receive brain coil (8HRBRAIN, General Electric Medical Systems).

SNR values were determined as the ratio of the mean signal intensity and the standard deviation of the noise. The mean signal was calculated in a region of interest (ROI) of a homogeneous region at the center of the image. The standard deviation of the noise was determined in a ROI in the background of the image.

PIQUE is a blind image quality assessment method which does not require prior information about the type of distortion. Lower quality score (Qscore) implies less distortion and thus, better image quality. The Qscore was evaluated in a middle slice of the acquisition plane.

2.5 | In vivo experiments

Human in vivo experiments were carried out to assess the image quality of the different CSPI sampling patterns on 3D-GRASE and 3D-FSE sequences. The study was approved by our Institutional Review Board and informed consent was obtained from the volunteers. The images from four volunteers were acquired, two for brain and two for knee. The same MR system as for the phantom experiments was used for the acquisitions, with an eight-channel phase-array transmit-receive knee coil (Precision Eight TX/TR High-Resolution Knee Array, In Vivo, Orlando, Florida) for knee PD-weighted and an eight-channel birdcage-like receive brain coil (8HRBRAIN, General Electric Medical Systems) for brain T_2-weighted. The parameters for each protocol are shown in Table 1 for PD-weighted acquisitions and Table 2 for T_2-weighted acquisitions. Images were acquired in the sagittal plane with frequency encoding direction S/I.

As in phantom experiments, SNR and Qscore were evaluated from the images of the volunteers. For SNR measurements on knee images, the mean signal intensity was

calculated in the synovial fluid and for the brain images, the mean signal intensity was calculated in the cerebrospinal fluid. In both, the standard deviation of the noise was calculated in an ROI on the background of the image. The Qscore was evaluated in a middle slice of the acquisition plane (sagittal plane).

For each sequence, the average whole body SAR (AveSAR), in W/Kg was obtained from the scanner's reported values. Briefly, each active RF pulse in the sequence is normalized to a quantity of standardized RF pulses (1 millisecond long, 180° flip angle), where the B1 field is known (0.117 G). Afterward, all RF pulses in one TR are summed together:

$$\text{stdrf} = \Sigma_{\text{pulses}} \left(\frac{\gamma B1}{0.117\gamma} \right)^2 \left(\frac{PW_{\text{pulse}}}{1\ \text{millisecond}} \right), \quad (3)$$

where γ is the gyromagnetic ratio, B1 is the effective B1 field value produced by the RF pulse, PW_{pulse} is the pulse width (in milliseconds) that the standardized RF rectangular pulse would be if it had an identical area as the absolute value of the pulse under consideration.

After, for the eight-channel birdcage-like receive brain coil, the average whole body SAR is obtained by:

$$\text{AveSAR} = \frac{\text{stdrf} * \text{jstd}}{\text{weight} * \text{TR}}, \quad (4)$$

where jstd is the energy deposited in the subject calculated from a curve calibrated to the system (in Joules), weight is the subject weight (in Kg), and TR is the repetition time of the sequence (in second). For the eight-channel phase-array transmit-receive knee coil, the whole body SAR is obtained replacing the weight in (4) by:

$$\text{CoilWeight} = 0.15\,(weight)^{0.67}, \quad (5)$$

where weight is the weight of the subject.

Reported AveSAR values in Tables 1 and 2 belong to volunteers with a weight of 70Kg.

3 | RESULTS

3.1 | Simulation experiments

Table 3 presents the values of the coherence of every sampling pattern evaluated for CSPI 3D-GRASE and CSPI 3D-FSE. No coherence values are shown for the PI acquisitions, since it is only relevant for CS reconstruction. In general, among the sampling patterns investigated the lowest coherence is obtained by sampling patterns combining a VD Poisson-disc k-space grid in both PD-weighted and T_2-weighted contrasts.

For CSPI 3D-GRASE, the lowest coherence is achieved for PD-weighted by the sampling patterns combining a VD Poisson-disc k-space grid with SRE $M = 0$ or SRE $M = 1$ trajectories, and for T_2-weighted by the sampling pattern combining a VD Poisson-disc k-space grid with SLE trajectory for both tissues. It can be observed that sampling patterns for 3D-GRASE PD-weighted with a VD Poisson-disc k-space grid obtain higher coherence when off-resonance effects are taking into account. From the coherence values of the different trajectories, it can be observed that they are mainly influenced by the chosen k-space grid. For 3D-GRASE T_2-weighted, the coherence value is constant with and without off-resonance effects. On the contrary, sampling patterns with a VD pseudo-random Gaussian k-space grid obtain lower coherence when off-resonance effects are considered in PD; however, for T_2, the coherence value is higher if off-resonance effects are considered. Coherence for CSPI 3D-FSE considering off-resonance effects is not different from not considering off-resonance effects, due to SE are not affected by off-resonance frequencies.

The resolution of every sampling pattern was evaluated by the FWHM. For PD, sampling patterns combining a VD pseudo-random Gaussian k-space grid obtain, in general, higher resolution for y and z. However, it also obtains higher sidelobes on the PSF than a VD Poisson-disc k-space grid, suggesting more artifacts on the images (see Supporting Information Figure S6 and Supporting Information Figure S7). For T_2, both k-space grids obtain similar FWHM measurements. Though, as in PD, a VD pseudo-random Gaussian k-space grid has higher sidelobes on the PSF than a VD Poisson-disc k-space grid. Moreover, the peak of the PSF for a VD pseudo-random Gaussian k-space grid along z is displaced (see Supporting Information Figure S8).

In general, CSPI increases the FWHM of the images compared to PI in both sequences and contrasts, especially for PD.

3.2 | Phantom experiment

Table 4 shows the SNR and Qscore of every sampling pattern and sequence for PD-weighted and T_2-weighted phantom images.

For PD-weighted images, the highest SNR is, in most of the cases, achieved by CSPI 3D-FSE acquisitions. Among sampling patterns for CSPI 3D-FSE, the VD pseudo-random Gaussian k-space grid with radial modulation achieves the highest SNR. Although PI 3D-FSE obtains lower SNR than CSPI, the Qscore indicates a higher image quality. In CSPI 3D-GRASE, sampling patterns with a VD Poisson-disc k-space grid and VD pseudo-random Gaussian k-space grid achieve the highest SNR for the SLCE 2 trajectory. In general, a higher image quality (lower Qscore) is achieved by sampling patterns with lower SNR, except for the SLCE 2 trajectory. In the phantom acquisition, the best compromise between SNR and Qscore among CSPI 3D-GRASE sampling patterns, as in PI 3D-GRASE, is achieved by VD pseudo-random Gaussian k-space grid with SLCE 2 trajectory. Figure 2 shows the phantom images, in sagittal and axial planes,

TABLE 3 Coherence and full width at half maximum (FHWM) measurements for the proposed PD-weighted and T_2-weighted sampling patterns for CSPI and PI

			Sampling Pattern		Coherence		FWHM (voxels)			
							CL		BM	
Contrast	Sequence		Grid	Trajectory	CL	BM	*y*	*z*	*y*	*z*
PD	FSE	CSPI	VD Poisson	Radial Mod.	0.25/0.25	0.19/0.19	1.8/1.8	1.6/1.6	1.4/1.4	1.2/1.2
			VD Gaussian	Radial Mod.	0.64/0.64	0.70/0.70	1.6 /1.6	1.6/1.6	1.2/1.2	1.2/1.2
		PI	Regular	Radial Mod.	-	-	1.2/1.2	1.2/1.2	1.0/1.0	1.0/1.0
	GRASE	CSPI	VD Poisson	SRE M = 0	0.31/0.35	0.21/0.28	1.4/1.6	1.2/1.4	1.2/1.6	1.4/1.6
				SRE $M = 1$	0.28/0.33	0.20/0.27	1.4/1.9	1.2/1.6	1.2/1.6	1.2/1.4
				SLCE 1	0.34/0.39	0.21/0.34	2.2/2.3	1.2/1.4	1.4/2.6	1.2/1.3
				SLCE 2	0.33/0.40	0.21/0.35	2.0/2.9	1.2/1.4	1.4/6.7	1.2/1.3
			VD Gaussian	SRE $M = 0$	0.63/0.59	0.69/0.66	1.2/1.5	1.2/1.6	1.0/1.4	1.0/1.3
				SRE $M = 1$	0.64/0.60	0.69/0.66	1.2/1.8	1.2/1.6	1.1/1.6	1.1/1.4
				SLCE 1	0.64/0.62	0.69/0.69	1.9/1.4	1.2/1.4	1.2/1.4	1.2/1.3
				SLCE 2	0.64/0.61	0.69/0.67	1.7/2.0	1.2/1.3	1.2/0.5	1.0/1.3
		PI	Regular	SRE $M = 0$	-	-	1.2/1.2	1.2/1.2	1.2/1.2	1.2/1.2
				SRE $M = 1$	-	-	1.0/1.2	1.0/1.2	1.2/1.2	1.2/1.2
				SLCE 1	-	-	1.0/1.4	1.0/1.4	1.2/1.0	1.0/1.5
				SLCE 2	-	-	1.0/2.8	1.0/1.5	1.2/3.2	1.1/2.0
					GM	WM	GM		WM	
							y	*z*	*y*	*z*
T_2	FSE	CSPI	VD Poisson	Linear Mod.	0.25/0.25	0.24/0.24	1.6/1.6	1.4/1.4	1.4/1.4	1.4/1.4
			VD Gaussian	Linear Mod.	0.54/0.54	0.54/0.54	1.3/1.3	1.2/1.2	1.2/1.2	1.2/1.2
		PI	Regular	Linear Mod.	-	-	1.6/1.6	1.2/1.2	1.4/1.4	1.2/1.2
	GRASE	CSPI	VD Poisson	SLE	0.25/0.25	0.23/0.23	1.5/1.1	1.4/1.4	1.4/1.4	1.4/1.4
			VD Gaussian	SLE	0.54/0.58	0.53/0.59	1.4/1.6	1.1/1.2	1.4/1.5	1.1/1.2
		PI	Regular	SLE	-	-	1.5/1.1	1.2/1.5	1.4/1.1	1.2/1.4

Four tissues were simulated: cartilage (CL) and bone marrow (BM) for PD-weighted knee, and gray matter (GM) and white matter (WM) for T_2-weighted brain. The coherence and FWHM were obtained for the different tissues without and with off-resonance effects, denote in the table by a slash (B0 = 0 Hz/B0 = 50 Hz). VD Poisson stands for variable density Poisson-disc, VD Gaussian stands for variable density pseudo-random Gaussian.

TABLE 4 SNR and Qscore measurements in a phantom and two volunteers for CSPI 3D-FSE, PI 3D-GRASE, CSPI 3D-GRASE and PI 3D-GRASE

			Sampling Pattern		Phantom		Volunteer 1		Volunteer 2	
Contrast	**Sequence**		**K-space grid**	**Trajectory**	**SNR**	**Qscore**	**SNR**	**Qscore**	**SNR**	**Qscore**
PD	FSE	CSPI	VD Poisson	Radial Mod.	131.49	43.44	181.11	35.21	112.07	35.60
			VD Gaussian	Radial Mod.	152.96	44.09	164.86	36.46	101.03	37.37
		PI	Regular	Radial Mod.	95.54	40.79	125.19	39.07	102.75	40.04
	GRASE	CSPI	VD Poisson	SRE $M = 0$	38.79	43.58	143.32	35.27	77.92	32.56
				SRE $M = 1$	45.71	43.50	210.70	36.59	101.85	34.18
				SLCE 1	47.87	39.14	80.78	32.81	60.84	32.65
				SLCE 2	87.83	41.41	116.95	33.46	79.46	32.40
			VD Gaussian	SRE M = 0	33.04	43.12	134.65	35.58	61.74	31.98
				SRE $M = 1$	49.33	42.54	121.14	39.91	78.11	33.79
				SLCE 1	40.34	38.61	71.84	33.36	38.14	32.54
				SLCE 2	154.30	42.24	93.84	33.62	62.71	32.82
		PI	Regular	SRE M = 0	42.12	40.36	96.50	36.16	115.49	39.79
				SRE $M = 1$	44.11	41.07	104.71	35.15	77.35	37.94
				SLCE 1	45.76	35.66	66.38	34.39	109.62	38.63
				SLCE 2	35.49	36.55	109.01	35.15	55.70	36.6
T_2	FSE	CSPI	VD Poisson	Linear Mod.	29.85	63.79	241.39	41.75	250.60	45.96
			VD Gaussian	Linear Mod.	32.34	64.57	372.88	44.08	235.96	47.23
		PI	Regular	Linear Mod.	55.33	75.76	152.05	42.72	159.54	49.60
	GRASE	CSPI	VD Poisson	SLE	46.85	64.71	130.25	42.31	109.79	44.56
			VD Gaussian	SLE	48.56	66.71	96.24	42.45	115.02	42.80
		PI	Regular	SLE	32.90	75.67	97.81	41.49	132.56	43.31

VD Poisson stands for variable density Poisson-disc, VD Gaussian stands for variable density pseudo-random Gaussian.

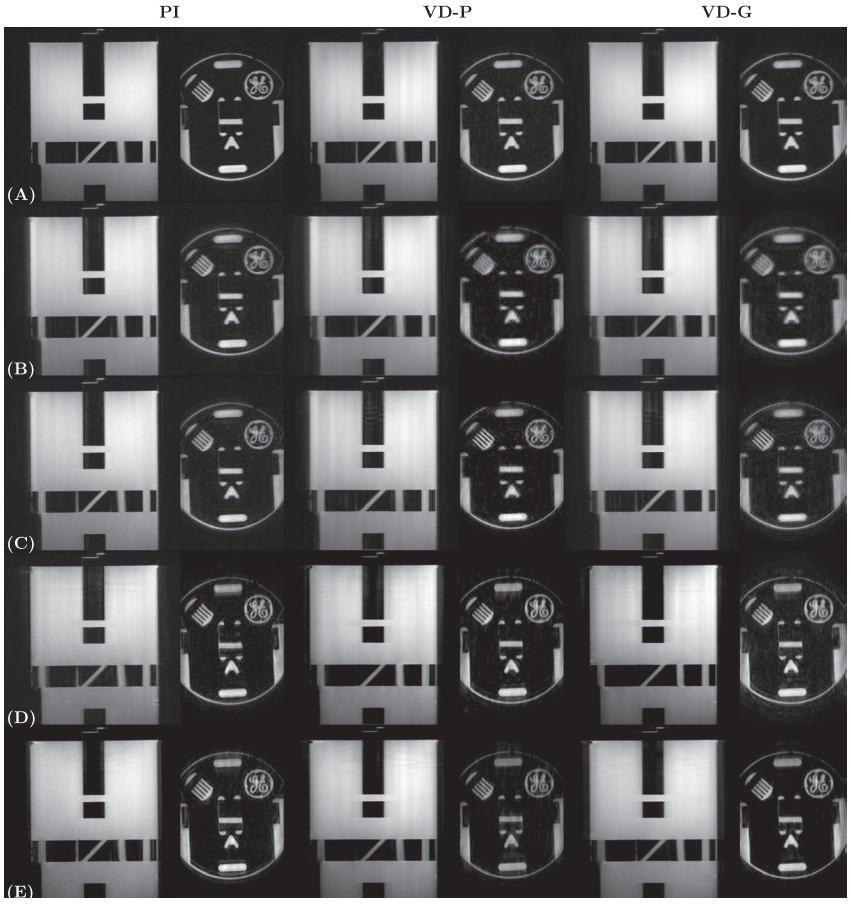

FIGURE 2 PD-weighted phantom images for 3D-FSE and 3D-GRASE with the proposed sampling patterns. Each row shows a different trajectory: (A), 3D-FSE with radial trajectory, (B), 3D-GRASE with SRE = 0, (C), 3D-GRASE with SRE = 1, (D), 3D-GRASE with SLCE 1, (E), 3D-GRASE with SLCE 2. Each column pair shows a different k-space grid: PI k-space grid, CSPI VD Poisson-disc undersampled k-space grid (VD-P) and the VD pseudo-random Gaussian undersampled k-space grid (VD-G). The sagittal and axial planes are shown for every k-space grid

acquired by 3D-FSE and 3D-GRASE with every sampling pattern and acceleration technique (PI and CSPI). PI 3D-FSE obtains the most sharp image, with no artifacts, as it is reported by its low Qscore. We can also appraise that the axial plane shows strong blurring artifacts for the sampling pattern combining a VD Poisson-disc with the SLCE 2 trajectory.

For T_2-weighted images, the highest SNR is achieved by the PI 3D-FSE acquisition, while CSPI 3D-FSE, PI 3D-GRASE, and CSPI 3D-GRASE acquisitions reduce the SNR about 15%. Among CSPI sampling patterns, the highest SNR is achieved by the VD pseudo-random Gaussian for both 3D-FSE and 3D-GRASE. The Qscore measurement shows that PI obtains lower image quality than CSPI acquisitions. Among sampling patterns, the highest image quality is obtained by the VD Poisson-disc k-space grid for CSPI 3D-FSE and for CSPI 3D-GRASE. The differences in Qscore among sampling patterns for CSPI are small, while between acceleration techniques (PI and CSPI) are moderate. Figure 3 shows the phantom images acquired by 3D-FSE and 3D-GRASE with every sampling pattern and acceleration

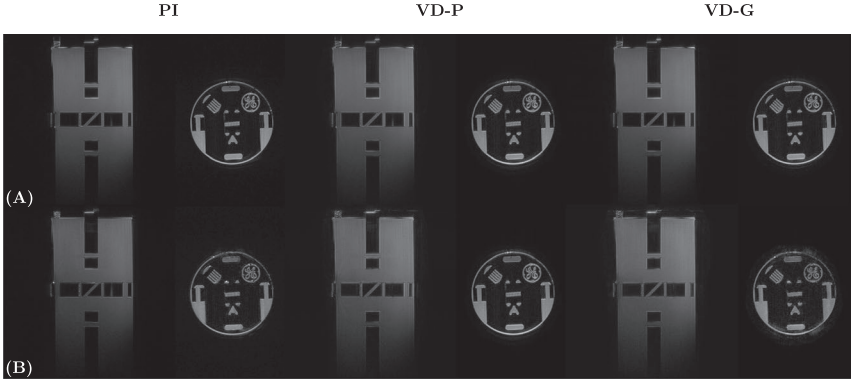

FIGURE 3 T_2-weighted phantom images for 3D-FSE and 3D-GRASE with the proposed sampling patterns. Each row shows a different trajectory: (A), 3D-FSE with linear trajectory, (B), 3D-GRASE with SLE trajectory. Each column pair shows a different k-space grid: PI k-space grid, CSPI VD Poisson-disc undersampled k-space grid (VD-P), and the VD pseudo-random Gaussian undersampled k-space grid (VD-G). The sagittal and axial planes are shown for every k-space grid

technique (PI and CSPI). For CSPI, both sampling patterns obtain equivalent image quality.

3.3 | In vivo experiments

As for phantom experiments, Table 4 shows the SNR and Qscore of every sampling pattern and sequence for PD-weighted knee images and T_2-weighted brain images.

For PD-weighted knee images, PI and CSPI acquisitions achieve, in general, comparable SNR among the different sampling patterns. The highest SNR is achieved by a different sampling pattern in each volunteer. In general, CSPI 3D-FSE obtains the highest SNR compared to the sampling patterns proposed for CSPI 3D-GRASE. Among the sampling patterns proposed for CSPI 3D-GRASE, those using a VD Poisson-disc k-space grid achieve higher SNR for each trajectory. CSPI obtains comparable image quality than PI for both sequences. For both volunteers, the lowest Qscore is achieved by the sampling patterns combining the SLCE 1 or SLCE 2 trajectories. Taking into account the SNR and Qscore measurements, sampling patterns including a VD Poisson-disc k-space grid obtains the best image quality, since they obtain higher SNR with low Qscore. Specifically, the sampling patterns combining a VD Poisson-disc k-space grid with the SLCE 1 or SLCE 2 trajectory obtain the highest SNR with a low Qscore. CSPI 3D-GRASE reduces the acquisition time by 43% compared to a CSPI 3D-FSE acquisition. Figures 4 and 5 shows the

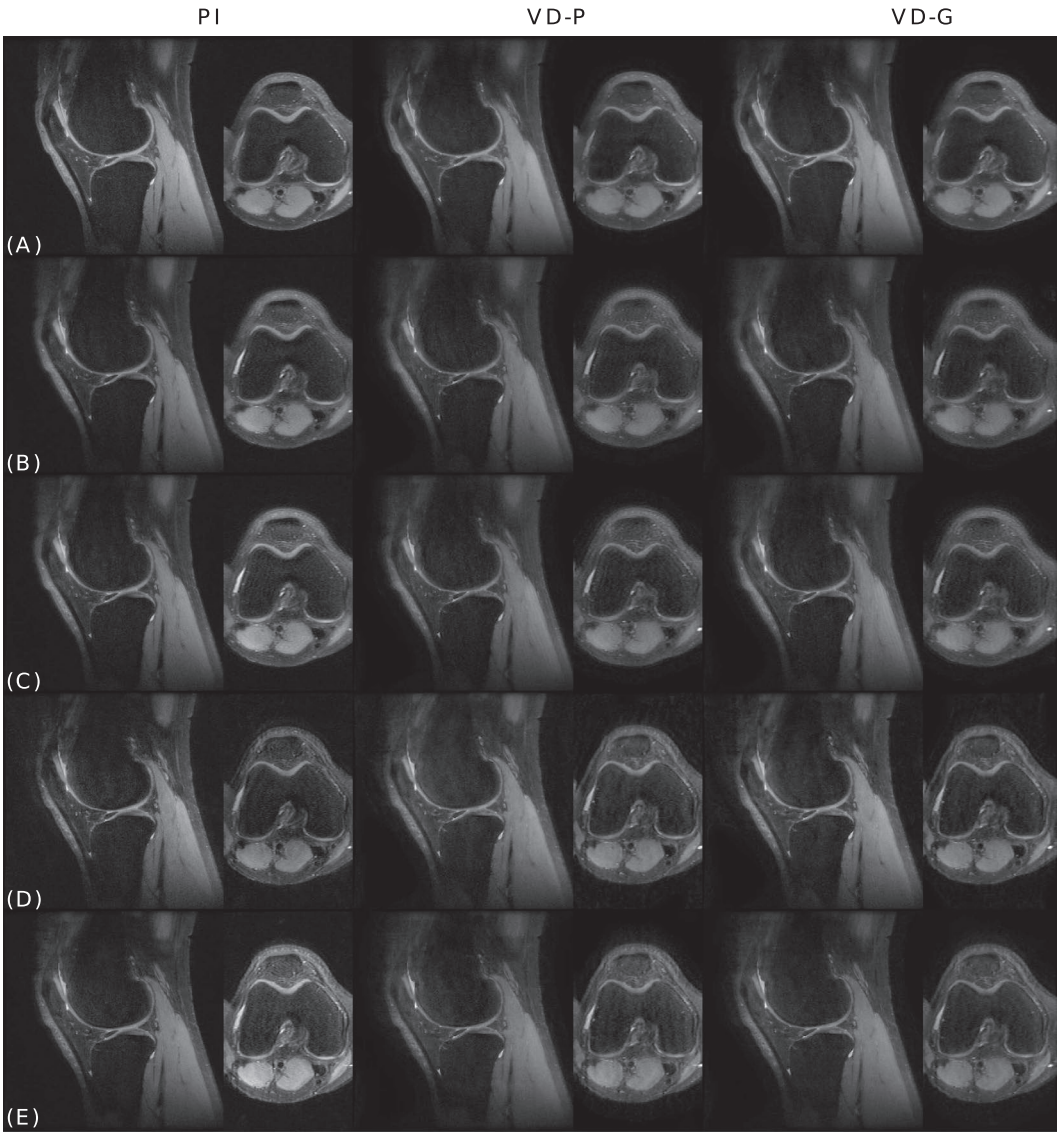

FIGURE 4 PD-weighted knee images of the first volunteer for 3D-FSE and 3D-GRASE with the proposed sampling patterns. Two orthogonal scan planes are shown every two columns: sagittal and axial. From left to right, the column pairs show the PI, the VD Poisson-disc undersampled k-space grid (VD-P), and the VD pseudo-random Gaussian undersampled k-space grid (VD-G). The different trajectories are shown in each row: (A), 3D-FSE with radial trajectory, (B), 3D-GRASE with SRE = 0, (C), 3D-GRASE with SRE = 1, (D), 3D-GRASE with SLCE 1, (E), 3D-GRASE with SLCE 2

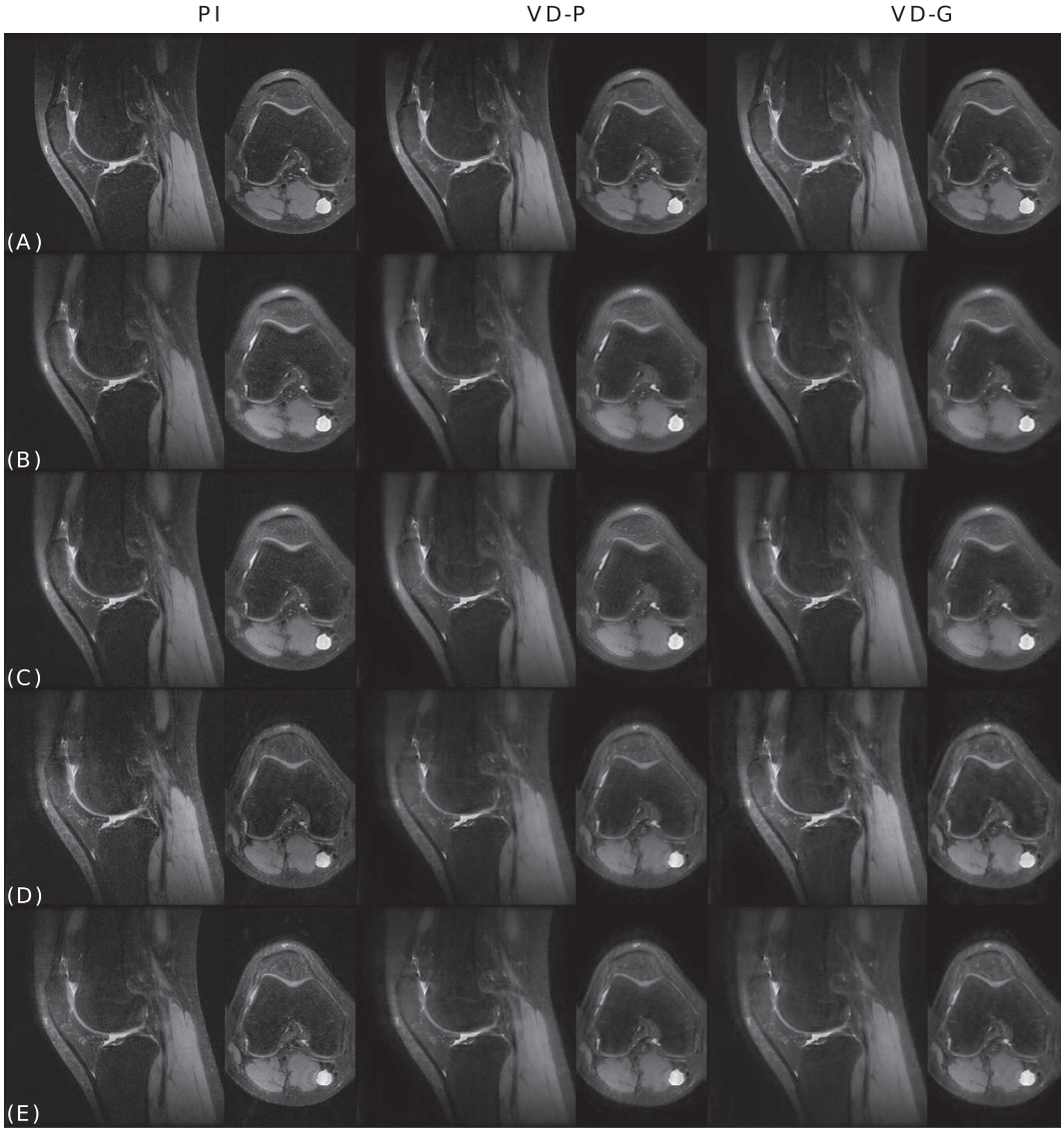

FIGURE 5 PD-weighted knee images of the second volunteer with the proposed sampling patterns. Two orthogonal scan planes are shown every two columns: sagittal and axial. From left to right, the column pairs show the PI, the VD Poisson-disc undersampled k-space grid (VD-P), and the VD pseudo-random Gaussian undersampled k-space grid (VD-G). The different trajectories are shown in each row: (A), 3D-FSE with radial trajectory, (B), 3D-GRASE with SRE = 0, (C), 3D-GRASE with SRE = 1, (D), 3D-GRASE with SLCE 1, (E), 3D-GRASE with SLCE 2

in vivo knee images for the first and the second volunteers, respectively, obtained with the different sampling patterns proposed for 3D-FSE and 3D-GRASE, both for PI and CSPI accelerated acquisitions. CSPI 3D-GRASE with the sampling patterns combining a VD Poisson-disc k-space grid with the SLCE 1 or the SLCE 2 trajectories obtain higher image quality than CSPI 3D-FSE (see Supporting Information Figure S9 and Supporting Information Figure S10).

For T_2-weighted brain images, CSPI acquisitions achieve the highest SNR among the acceleration techniques. The Qscore shows better image quality for CSPI 3D-GRASE than for CSPI 3D-FSE. This can be due to the lower SNR of 3D-GRASE, since less artifacts could be discerned. According to the measurements performed in in vivo T_2-weighted acquisitions, there is almost no difference among sampling patterns for CSPI 3D-GRASE and CSPI 3D-FSE in both volunteers, although the VD Poisson-disc k-space grid obtains significant higher SNR in volunteer 1. As in PD-weighted acquisitions, CSPI 3D-GRASE reduces the acquisition time by 40% compared to a CSPI 3D-FSE acquisition. Figure 6 shows the in vivo T_2-weigted brain images obtained for both volunteers with the different sampling patterns proposed for 3D-FSE and 3D-GRASE, both for PI and CSPI accelerated acquisitions. These images show that there is no clear artifacts or image degradation when CSPI is used (see also Supporting Information Figure S11).

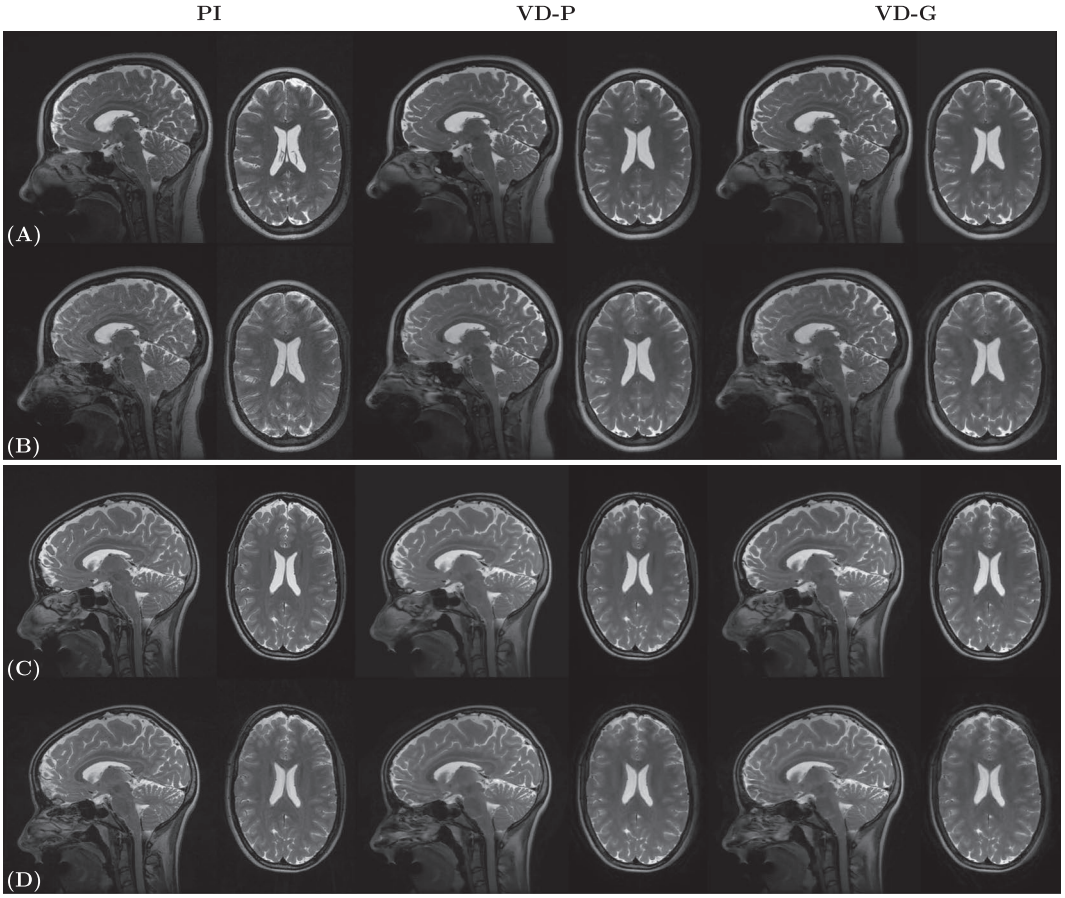

FIGURE 6 T_2-weighted brain images for the first and second volunteers with PI 3D-FSE, CSPI 3D-FSE, PI 3D-GRASE, and CSPI 3D-GRASE with the proposed sampling patterns. Two orthogonal scan planes are shown every two columns: sagittal and axial. From left to right, the column pairs show the PI, VD Poisson-disc undersampled k-space grid (VD-P) and the VD pseudo-random Gaussian undersampled k-space grid (VD-G). Each row shows a different trajectory: (A), 3D-FSE with linear trajectory, (B), 3D-GRASE with SLE trajectory for the first volunteer, and (C), 3D-FSE with linear trajectory, (D), 3D-GRASE with SLE trajectory for the second volunteer

4 | DISCUSSION

In this work, we presented and investigated a CSPI acquisition scheme for a 3D-GRASE sequence. To this end, ten CSPI k-space sampling strategies to accelerate the acquisition of 3D-GRASE were analyzed, eight for PD-weighted knee images and two for T_2-weighted brain images. PI images with every sequence were also analyzed and used as reference.

In CSPI, the coherence of the sampling pattern is, theoretically, one of the main elements influencing the reconstruction performance. The SPR showed that the lowest degree of coherence was obtained for sampling patterns combining a VD Poisson-disc k-space grid in PD-weighted and T_2-weighted contrasts for both CSPI 3D-GRASE and CSPI 3D-FSE sequences. Based on this fact, a better image quality could be expected than from sampling patterns combining a VD Poisson-disc k-space. Additionally, the differences in coherence among the trajectories for the different sampling patterns are small, suggesting that the trajectory has low influence on the coherence. Thus, the undersampling pattern of the k-space grid is the most important factor in terms of coherence. Nevertheless, the trajectory plays an important role for the image quality in 3D-GRASE acquisitions. Depending on the trajectory, different artifacts may be appraised in the images, as previously shown for accelerated high-resolution images,[6] since every trajectory modulates T_2 and T_2^* effects differently. Phantom and in vivo experiments showed that the coherence measurement cannot totally predict the final image quality. One of the reasons is that the simulations performed do not take into account all the effects that can happen in a real acquisition, as for example, eddy currents.

For PD-weighted images, the sampling patterns combining a VD Poisson-disc k-space grid with the SLCE 1 or SLCE 2 obtains one of the worse FWHM values along y among the trajectories, especially for off-resonance effects. Also,

we found that phantom images with the sampling pattern combining a VD Poisson-disc k-space grid with the SLCE 2 trajectory shows blur in the axial plane. However, we have not appraised this issue in in vivo knee images. The different properties of the phantom can cause different artifacts than expected in tissues. Though, compared to the other sampling pattern investigated, these sampling pattern obtain images where the cartilage can be clearly differentiated from the rest of the structures in the orthogonal planes. This demonstrates that prospective acquisitions are needed to fully investigate and evaluate CSPI acquisitions. Moreover, in PD-weighted knee imaging, CSPI loses some details of the patellar bone marrow compared to PI, both in 3D-FSE and 3D-GRASE.

For T_2-weighted images, SNR and Qscore showed that there is almost no difference in image quality between trajectories, although a VD pseudo-random Gaussian with the SLE trajectory obtains a slightly higher SNR in most of the cases. Simulations showed that the resolution, measured by the FWHM, is generally higher for sampling patterns including a VD pseudo-random Gaussian k-space grid when off-resonance effects are taking into account for CSPI 3D-FSE and for CSPI 3D-GRASE. Based on the FWHM, VD pseudo-random Gaussian k-space grids are less sensitive to off-resonance effects in 3D-GRASE and they should be used for CSPI 3D-GRASE acquisitions. However, we did not identify a loss of image resolution or more artifacts in WM for the sampling pattern including a VD Poisson-disc k-space as was predicted by the FHWM simulations.

An increase of the SNR in CSPI compared to PI was also found in this study. Although, in general 3D-GRASE reduces the SNR, since lower signal amplitudes are achieved by GRE, different reconstruction algorithms were used for PI and CSPI, which may be the cause of higher SNR in CSPI.

There were slight differences in TE among the acquisitions with different sampling patterns and sequences. Even though changes in TE may slightly affect the SNR and Qscore, it is not expected to influence the conclusions.

It is worth to mention that different ACS region sizes and shapes can influence image artifacts and, especially, acquisition time. For this work, a square ACS region was chosen since the BART library used to generate the Poisson-disc k-space only allows to create a square ACS region. The effect of the size and shape of the ACS region on the image quality of the different sampling patterns was not studied. In the same way, the effect of size and shape of the regular k-space area in the VD pseudo-random Gaussian k-space grid was not studied. Nevertheless, ACS size and shape differences are expected to impact PI and CSPI acquisitions in the same way. Additionally, the image quality of 3D-GRASE with a higher EPI factor has not been investigated in this work. For the applications considered in this paper (high-resolution structural imaging), a higher EPI factor is not recommendable, since it would increase the RF-spacing, obtaining blurrier images.

The image quality of the proposed CSPI 3D-GRASE acquisitions is similar to CSPI 3D-FSE, with the advantage that CSPI 3D-GRASE reduces the scan time by 43% for PD-weighted images and by 40% for T_2-weighted images. Although the images of CSPI 3D-GRASE acquisitions are slightly more blurred than PI acquisitions, the scan time reduction achieved may enable high-resolution 3D imaging to be rapidly incorporated in conventional clinical protocols.

5 | CONCLUSIONS

CSPI 3D-GRASE significantly reduces acquisition time compared to a CSPI 3D-FSE acquisition and can reduce SAR in clinical protocols. The design of the sampling pattern, including both the k-space grid and the k-space trajectory, is crucial to obtain high image quality in a high-resolution CSPI 3D-GRASE acquisition.

This work identifies several suitable undersampled k-space grid and trajectory combinations. Overall, we propose to use a VD Poisson-disc k-space grid with the SLCE 1 trajectory for PD-weighted knee imaging and a VD pseudo-random Gaussian k-space grid with the SLE trajectory for brain T_2-weighted imaging with CSPI 3D-GRASE.

ACKNOWLEDGMENTS

This work was partially supported by a General Electric Healthcare research grant.

REFERENCES

1. Yamabe E, Anavim A, Sakai T, et al. Comparison between high-resolution isotropic three-dimensional and high-resolution conventional two-dimensional FSE MR images of the wrist at 3 tesla: a pilot study. *J Magn Reson Imaging* 2014;40:603–608.
2. Mugler JP. Optimized three-dimensional fast-spin-echo MRI. *J Magn Reson Imaging* 2014;39:745–767.
3. Kemper VG, De Martino F, Yacoub E, Goebel R. Variable flip angle 3D-GRASE for high resolution fMRI at 7 tesla. *Magn Reson Med*. 2016;76:897–904.
4. Oshio K, Feinberg DA. GRASE (Gradient-and Spin-Echo) imaging: a novel fast MRI technique. *Magn Reson Med*. 1991;20:344–349.
5. Jovicich J, Norris DG. GRASE imaging at 3 Tesla with template interactive phase–encoding. *Magn Reson Med*. 1998;39:970–979.
6. Cristobal-Huerta A, Poot DH, Vogel MW, Krestin GP, Hernandez-Tamames JA. K-space trajectories in 3D-GRASE sequence for high resolution structural imaging. *Magn Reson Imaging* 2018;48:10–19.
7. Deshmane A, Gulani V, Griswold MA, Seiberlich N. Parallel MR imaging. *J Magn Reson Imaging* 2012;36:55–72.
8. Lustig M, Donoho DL, Santos JM, Pauly JM. Compressed sensing MRI. *IEEE Signal Process Mag*. 2008;25:72–82.
9. King K. Combining compressed sensing and parallel imaging. In Proceedings of the 16th Annual Meeting of ISMRM, Toronto, Canada, 2008:1488.

10. Otazo R, Kim D, Axel L, Sodickson DK. Combination of compressed sensing and parallel imaging for highly accelerated first-pass cardiac perfusion MRI. *Magn Reson Med*. 2010;64:767–776.
11. Pandit P, Rivoire J, King K, Li X. Accelerated T_{1_ρ} acquisition for knee cartilage quantification using compressed sensing and data-driven parallel imaging: a feasibility study. *Magn Reson Med*. 2016;75:1256–1261.
12. Cristobal-Huerta A, Poot DHJ, Vogel M, Hernandez-Tamames JA. Compressed Sensing 3D GRASE for Faster PD-weighted Knee Imaging. In Proceedings of the 25th annual meeting of ISMRM, Honolulu, HI; 2017:5020.
13. Cristobal-Huerta A, Poot DHJ, Vogel M, Hernandez-Tamames JA. Compressed Sensing Variable Flip Angle 3D-GRASE for T_2-weighted High-Resolution Brain Images. In Proceedings of the 34th Annual Meeting of ESMRMB, Barcelona; 2017:184.
14. Chan RW, Ramsay EA, Cheung EY, Plewes DB. The influence of radial undersampling schemes on compressed sensing reconstruction in breast MRI. *Magn Reson Med*. 2012;67:363–377.
15. Liu DD, Liang D, Liu X, Zhang YT. Under-sampling trajectory design for compressed sensing MRI. Conf Proc IEEE Eng Med Biol Soc., San Diego, CA; 2012:73–76.
16. Levine E, Daniel B, Vasanawala S, Hargreaves B, Saranathan M. 3D Cartesian MRI with compressed sensing and variable view sharing using complementary poisson-disc sampling. *Magn Reson Med*. 2017;77:1774–1785.
17. Zijlstra F, Viergever MA, Seevinck PR. Evaluation of variable density and data-driven k-space undersampling for compressed sensing magnetic resonance imaging. *Invest Radiol*. 2016;51:410–419.
18. Bilgic B, Goyal VK, Adalsteinsson E. Multi-contrast reconstruction with Bayesian compressed sensing. *Magn Reson Med*. 2011;66:1601–1615.
19. Tamir JI, Ong F, Cheng JY, Uecker M, Lustig M. Generalized magnetic resonance image reconstruction using the Berkeley Advanced Reconstruction Toolbox. ISMRM Workshop on Data Sampling & Image Reconstruction, Sedona, AZ; 2016.
20. Mugler JP. Improved three-dimensional GRASE imaging with the SORT phase-encoding strategy. *J Magn Reson Imaging* 1999;9:604–612.
21. Busse RF, Brau A, Vu A, et al. Effects of refocusing flip angle modulation and view ordering in 3D fast spin echo. *Magn Reson Med*. 2008;60:640–649.
22. Lai P, Lustig M, Brau A, Vasanawala S, Beatty P, Alley M. Efficient L1-SPIRiT reconstruction (ESPIRiT) for highly accelerated 3d volumetric MRI with parallel imaging and compressed sensing. In Proceedings of the 18th Annual Meeting of ISMRM, Stockholm, Sweden; 2010:345.
23. Brau A, Beatty P, Skare S, Bammer R. Efficient computation of autocalibrating parallel imaging reconstruction. Proceedings of the 14th Annual Meeting of ISMRM, Seattle, Washington; 2006: 2462.
24. Lustig M, Donoho D, Pauly JM. Sparse MRI: The application of compressed sensing for rapid MR imaging. *Magn Reson Med*. 2007;58:1182–1195.
25. Wansapura JP, Holland SK, Dunn RS, Ball WS Jr. NMR relaxation times in the human brain at 3.0 tesla. *J Magn Reson Imaging* 1999;9:531–538.
26. Lu H, Nagae-Poetscher LM, Golay X, Lin D, Pomper M, Van Zijl PC. Routine clinical brain MRI sequences for use at 3.0 Tesla. *J Magn Reson Imaging* 2005;22:13–22.
27. Han E, Gold G, Stainsby J, Wright G, Beaulieu C, Brittain J. In-vivo T_1 and T_2 measurements of muskuloskeletal tissue at 3T and 1.5T. In Proceedings of the 11th annual meeting of ISMRM, Toronto, Canada; 2003:450.
28. Weinreb J, Wilcox PA, Hayden J, Lewis R, Froelich J. ACR MRI accreditation: yesterday, today, and tomorrow. *J Am Coll Radiol*. 2005;2:494–503.
29. Venkatanath N, Praneeth D, Bh MC, Channappayya SS, Medasani SS. Blind image quality evaluation using perception based features. 2015 Twenty First National Conference on Communications (NCC), Mumbai, India; 2015:1–6.

SUPPORTING INFORMATION

Additional supporting information may be found online in the Supporting Information section at the end of the article.

FIGURE S1 CSPI 3D-GRASE sampling patterns for PD-weighted images with the SRE $M = 0$ trajectory: (A), VD Poisson-disc undersampled k-space grid and (B), VD pseudo-random Gaussian undersampled k-space grid. The EPI factor is set to 3. The different marker shapes indicate the different echo types: square for GRE before the SE, circle symbol for SE, and triangle for GRE after SE. The colormap represents the order in the acquisition of every echo along the ET. Transparency indicates the train number in which the k-space line is acquired, increasing for higher train numbers

FIGURE S2 CSPI 3D-GRASE sampling patterns for PD-weighted images with the SRE $M = 1$ trajectory: (A), VD Poisson-disc undersampled k-space grid and (B), VD pseudo-random Gaussian undersampled k-space grid. The EPI factor is set to 3. The different marker shapes indicate the different echo types: square for GRE before the SE, circle symbol for SE, and triangle for GRE after SE. The colormap represents the order in the acquisition of every echo along the ET. Transparency indicates the train number in which the k-space line is acquired, increasing for higher train numbers

FIGURE S3 CSPI 3D-GRASE sampling patterns for PD-weighted images with the SLCE 1 trajectory: (A), VD Poisson-disc undersampled k-space grid and (B), VD pseudo-random Gaussian undersampled k-space grid. The EPI factor is set to 3. The different marker shapes indicate the different echo types: square for GRE before the SE, circle symbol for SE, and triangle for GRE after SE. The colormap represents the order in the acquisition of every echo along the ET. Transparency indicates the train number in which the k-space line is acquired, increasing for higher train numbers

FIGURE S4 CSPI 3D-GRASE sampling patterns for PD-weighted images with the SLCE 2 trajectory: (A), VD Poisson-disc undersampled k-space grid and (B), VD pseudo-random Gaussian undersampled k-space grid. The EPI factor is set to 3. The different marker shapes indicate the different echo types: square for GRE before the SE, circle

symbol for SE, and triangle for GRE after SE. The colormap represents the order in the acquisition of every echo along the ET. Transparency indicates the train number in which the k-space line is acquired, increasing for higher train numbers

FIGURE S5 CSPI 3D-GRASE sampling patterns for T_2-weighted images with the SLE trajectory: (A), VD Poisson-disc undersampled k-space grid and (B), VD pseudo-random Gaussian undersampled k-space grid. The EPI factor is set to 3. The different marker shapes indicate the different echo types: square for GRE before the SE, circle symbol for SE. and triangle for GRE after SE. The colormap represents the order in the acquisition of every echo along the ET. Transparency indicates the train number in which the k-space line is acquired, increasing for higher train numbers

FIGURE S6 PSF for PD-weighted PI 3D-FSE and PI 3D-GRASE with each sampling pattern. Each column shows the PSF along *y* and *z* for: (A), 3D-FSE radial modulation, (B), PI and CSPI 3D-GRASE SRE $M = 0$, (C), 3D-GRASE SRE $M = 1$, (D), 3D-GRASE SCLE 1 and (E) 3D-GRASE SCLE 2

FIGURE S7 PSF for PD-weighted CSPI 3D-FSE and CSPI 3D-GRASE with each sampling pattern. Each pair of columns show the PSF along *y* and *z* for the VD Poisson-disc undersampled k-space grid (VD-P) and the VD pseudo-random Gaussian undersampled k-space grid (VD-G). Each row shows a different trajectory and sequence: (A), 3D-FSE radial modulation, (B), 3D-GRASE SRE $M = 0$, (C), PI and CSPI 3D-GRASE SRE $M = 1$, (D), 3D-GRASE SCLE 1 and (E), 3D-GRASE SCLE 2

FIGURE S8 PSF for T_2-weighted PI 3D-FSE, CSPI 3D-FSE, PI 3D-GRASE, and CSPI 3D-FSE with each sampling pattern. Columns show the PSF along *y* and *z* for PI, the VD Poisson-disc undersampled k-space grid (VD-P) and the VD pseudo-random Gaussian undersampled k-space grid (VD-G): (A), PI 3D-FSE and CSPI 3D-FSE linear modulation, (B), PI and CSPI 3D-GRASE SLE

FIGURE S9 Zoomed PD-weighted knee images for 3D-FSE and 3D-GRASE with the proposed sampling patterns for the first volunteer. Cartilage is zoomed in the sagittal plane. Each column shows the parallel imaging (PI) images, CSPI VD Poisson-disc undersampled k-space grid (VD-P), and the CSPI VD pseudo-random Gaussian undersampled k-space grid (VD-G). The different trajectories are shown in each row: (A), 3D-FSE with radial trajectory, (B), 3D-GRASE with SRE = 0, (C), 3D-GRASE with SRE = 1, (D), 3D-GRASE with SLCE 1, (E), 3D-GRASE with SLCE 2

FIGURE S10 Zoomed PD-weighted knee images for 3D-FSE and 3D-GRASE with the proposed sampling patterns for the second volunteer. Cartilage is zoomed in the sagittal plane. Each column shows the parallel imaging (PI) images, CSPI VD Poisson-disc undersampled k-space grid (VD-P) and the CSPI VD pseudo-random Gaussian undersampled k-space grid (VD-G). The different trajectories are shown in each row: (A), 3D-FSE with radial trajectory, (B), 3D-GRASE with SRE = 0, (C), 3D-GRASE with SRE = 1, (D), 3D-GRASE with SLCE 1, (E), 3D-GRASE with SLCE 2

FIGURE S11 Zoomed T_2-weighted brain images for CSPI 3D-FSE and CSPI 3D-GRASE with the proposed sampling patterns in the sagittal plane for the first and second volunteers. Each column shows the parallel imaging (PI) with linear trajectory, CSPI VD Poisson-disc undersampled kspace grid (VD-P), and the CSPI VD pseudo-random Gaussian undersampled k-space grid (VD-G). The first two rows show (A), 3D-FSE, (B), 3D-GRASE for the first volunteer. The two last rows show (C), 3D-FSE, (D), 3D-GRASE for the second volunteer

How to cite this article: Cristobal-Huerta A, Poot DHJ, Vogel MW, Krestin GP, Hernandez-Tamames JA. Compressed Sensing 3D-GRASE for faster High-Resolution MRI. *Magn Reson Med*. 2019;82: 984–999. https://doi.org/10.1002/mrm.27789